

# Contact Angle, Film and Line Tension of Foam Films.

## II. Film and Line Tension Measurements

A. S. DIMITROV, A. D. NIKOLOV, P. A. KRALCHEVSKY,  
AND I. B. IVANOV,<sup>1</sup>

*Laboratory of Thermodynamics and Physico-Chemical Hydrodynamics,  
University of Sofia, Faculty of Chemistry, Sofia 1126, Bulgaria*

Received April 15, 1991; accepted November 26, 1991

New experiments with air bubbles floating at the surface of aqueous solutions of sodium dodecyl sulfate have been carried out. At a given size the spontaneous shrinking of such a bubble has been stopped by regulating the pressure inside the cell. The relaxation of the contact line radius with time has been recorded by taking photographs. The film curvature was measured by utilizing a precise differential interferometric technique. The data allows independent calculation of the film and line tensions,  $\gamma$  and  $\kappa$ . For a "stopped" bubble both  $\gamma$  and  $\kappa$  relax with time:  $\kappa$  tends to zero and  $\gamma$  tends to its equilibrium value known from other experiments. The results suggest that for this system one can introduce the concept of *dynamic* line tension, which arises because of the motion of the contact line. This effect can be important in all cases when the interactions between fluid colloid particles and/or biological cells are accompanied with formation of a three-phase contact line. © 1992 Academic Press, Inc.

### 1. INTRODUCTION

The importance of the line tension for the interactions between small fluid particles in emulsions, foams, and biological systems is well recognized. On the other hand, the experimental information about the values of the line tension and its effect on the three-phase contact angles is still scanty and controversial. Some of the problems, connected with the measurement of the line tension are reviewed in Part I of the present study (Ref. (1)), where new experimental data for the contact angle of small floating bubbles were also presented. It was established that the shrinking of the contact line leads to a deviation of the contact angle from its equilibrium value. When the shrinking of a bubble has been arrested, the contact angle relaxes and reaches eventually its equilibrium value. This study is continued in the present paper. This time the relaxations of the film and line tensions,  $\gamma$  and  $\kappa$  are investigated experimentally. The additional ex-

perimental information needed for independent calculation of  $\gamma$  and  $\kappa$  is obtained by differential interferometric measurements of the curvature of the thin foam film at the bubble cap. Since the effect of  $\kappa$  is small, special attention is paid to the accuracy and reliability of this interferometric optical technique.

In the system studied by us the interfaces are fluid and the processes are very slow. That is why the surface roughness and the viscous flows have probably negligible effect.

### 2. EXPERIMENTAL PROCEDURE

The experimental cell with variable pressure and the materials used are described in Section 2 of Part I (Ref. (1)). That is why we give below only a description of the interferometric technique for measuring the radius of curvature  $R_f$  of the thin film at the cap of the bubble—Fig. 1.

The experiments were carried out with a differential microscope (Epival Interphako, Carl Zeiss, Jena) using objective ( $\times 12.5$ ). The light source was a high-pressure mercury lamp

<sup>1</sup> To whom correspondence should be addressed.

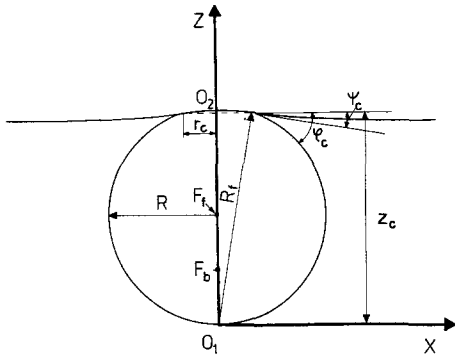


FIG. 1. Sketch of a small bubble attached to a liquid-gas interface;  $r_c$ ,  $R$ , and  $R_f$  are the radii of the contact line, bubble equator, and film curvature, respectively.

(HBO-50W) combined with a filter transmitting only the green spectral line of wavelength 546 nm. In order to produce an interference pattern of better contrast we used an illumination screen grid of constant  $48 \mu\text{m}$ , the same as in Ref. (2). The principle of the differential interferometry and the construction of the microscope are described in detail in Refs. (3, 4). The application of the shearing method for measuring curvature of fluid interfaces is given in Refs. (2, 5, 6).

A shearing distance  $d = 24 \mu\text{m}$  was fixed at the beginning of each experiment and was not changed during the experiment. A bubble was formed as described in Ref. (1) and the experimental cell was hermetically closed. Such a bubble shrinks spontaneously because of gas diffusion across the thin film. At a given size its shrinking was stopped by regulating the pressure inside the cell as described in Ref. (1). Then the relaxation of  $r_c$  and  $R_f$  at fixed  $R$  was studied.

We need the dependence of  $R$ ,  $r_c$ , and  $R_f$  on time  $t$ . The experimental information needed was obtained in the following way. At suitably chosen time intervals three consecutive photographs were taken one immediately after another at time moments  $t_1$ ,  $t_2$ , and  $t_3$ . At moments  $t_1$  and  $t_3$  photographs of the bubble, allowing the determination of its equatorial diameter, were taken in transmitted light. At the intermediate moment  $t_2$  a pho-

tograph of the differential interference pattern due to the monochromatic light reflected from the film and liquid surface surrounding it was taken. Exposure time of 7 s was used with a photographic film HR II Fuji of sensitivity 6 ASA.  $R_f(t_2)$  and  $r_c(t_2)$  were determined directly from this photograph, whereas the respective value of  $R$  was calculated from the dependence  $R(t)$  by means of the linear interpolation

$$R(t_2) = R(t_1) + \frac{R(t_3) - R(t_1)}{t_3 - t_1} (t_2 - t_1). \quad [1]$$

This procedure allows determination of  $R(t_2)$  with a good accuracy, because the data from independent visual measurements of  $R$  vs  $t$  correlate very well with a straight line within time intervals of the order of  $(t_3 - t_1)$ . After the disappearance of the studied shrinking bubble, the radius of curvature,  $R_0$ , at the top of the convex liquid meniscus in the cylindrical container with the solution was measured. For this purpose we used microscope objective ( $\times 6.3$ ) and after removing the upper glass cover of the cell we took a photograph of the differential interference pattern created by this convex meniscus. The role of the latter is to keep the bubble immobile at the center of the liquid surface.

A typical photograph of the differential interference pattern created by the cap of the bubble is presented in Fig. 2. Just as in Refs. (2, 7) three kinds of interference fringes, called the "streaks," "rings," and "moustaches," are observed. In comparison with the experiments in Ref. (2) we used a longer-distance objective ( $\times 12.5$ ), instead of ( $\times 25$ ), because of the presence of an upper glass cover on the experimental cell. The change of the objective led to the appearance of a greater number of streaks and rings than in Ref. (2).

As it is shown in Refs. (2, 7) the streaks are due to interference between the two images of the spherical film, whereas the rings are due to interference between the superimposed film and meniscus surfaces. One sees in Fig. 2 that

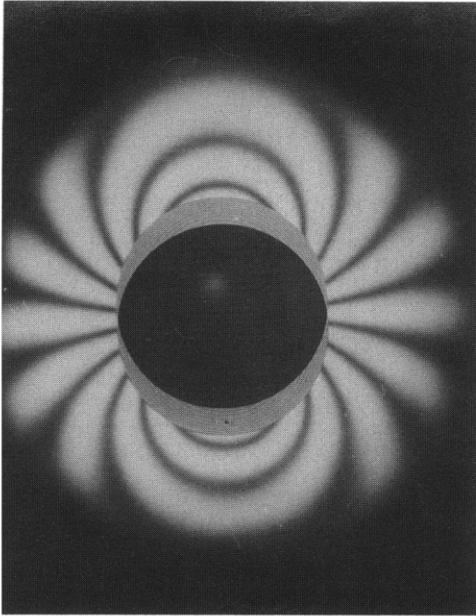


FIG. 2. Differential interference pattern in light reflected from the cap of a floating bubble and the liquid meniscus around it.

the streaks appear on a darker background than the rings. This can be explained by the higher reflectivity of the meniscus surfaces. It turns out that as a result of this the rings yield the value of  $R_f$  with better accuracy at shorter exposure times than the streaks. That is why in the present work we used the rings for calculating  $R_f$ . The better accuracy is achieved at the expense of more complicated calculations than in Ref. (2)—see below. In all cases when  $R_f$  was independently determined from streaks and rings on the same photograph, coincidence of the results was established in the framework of the experimental accuracy.

### 3. PROCESSING OF THE INTERFERENCE PATTERN

The procedure for calculation of  $R_f$  presented below is a generalization of a similar procedure published in Ref. (2). In general, the interferometric microscopes, like Epival Interphako, allow both “horizontal” and “vertical” splitting of the image. The “horizontal” splitting consists in the appearance of

two equivalent images displaced at a distance  $d$  from each other. The “vertical” splitting is realized by means of an optical wedge inside the Max-Zehnder interferometer built in the microscope. The position of the wedge can be changed by using a screw. This leads to changes in the positions of the dark and bright interference fringes. The “vertical” splitting can be represented schematically as a vertical shift,  $h$ , between the left- and right-hand side images of the reflecting surfaces—see Fig. 3. Because of the condition for interference this changes the positions of the fringes of different brightness. For example, a shift  $h = \lambda/8$  leads to an exchange of the dark fringes with bright ones and vice versa.

The origin of the coordinate system in Fig. 3 is chosen at the center of curvature of the left-hand side image. The horizontal splitting of magnitude  $d$  is along the  $X$  axis. The profiles of the left- and right-hand-side images are denoted by  $Z_l(x)$  and  $Z_r(x)$ , respectively. The fringes of maximum or minimum intensity are loci of points for which the distance between the reflecting surfaces satisfies the requirement

$$|Z_l - Z_r| = l_k \equiv k \frac{\lambda}{4}. \quad [2]$$

The order of interference  $k$  is odd for the dark fringes and even for the bright ones. The two spherical “caps” in Fig. 3 satisfy the equations

$$x^2 + Z_l^2 = R_f^2 \quad [3]$$

$$(x - d)^2 + (Z_r + h)^2 = R_f^2. \quad [4]$$

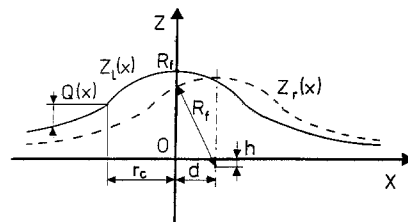


FIG. 3. A sketch of the cross-section of the reflecting surfaces shifted horizontally at a distance  $d$ , and vertically at distance  $h$ ;  $O$  is the center of curvature of the left-hand side bubble cap.

The elimination of  $Z_1$  and  $Z_r$  between Eqs. [2]–[4] yields the following expression for  $R_f$ :

$$R_f^2 = x_k^2 + \left[ \frac{(d - 2x_k)d + (1_k - h)^2}{2(1_k - h)} \right]^2 \quad [5]$$

Here  $x_k$  is the abscissa of the intersection point between the  $X$  axis and the  $k$ th streak. Equation [5] allows the calculation of  $R_f$  for each streak. The substitution  $x_k = x'_k + d/2$ ,  $h = 0$  reduces Eq. [5] to Eq. [10] in Ref. (2). In accordance with the least squares method the most probable value of  $R_f$  corresponds to a minimum of the function

$$\Phi(h) = \sum_{k=1}^N [\bar{R}_f - R_f(x_k; h)]^2,$$

where  $R_f(x_k; h)$  is calculated from Eq. [5] and

$$\bar{R}_f = \sum_{k=1}^N R_f(x_k; h)/N.$$

The summation is carried out over all streaks.

In our experiments the “vertical” splitting was adjusted manually to be zero, which makes the left- and right-hand-side parts of the interference pattern symmetrical. However, this adjustment cannot be perfect: this leads to a minimum value of  $\Phi(h)$  at some very small, but still nonzero, value of  $h$  ( $h \ll \lambda/8$ ).

It turned out that the computer minimization of  $\Phi(h)$  (as defined above) and of  $\Phi(a')$  as defined by Eq. [18] in Ref. (2) yields numerically coinciding results.

For the right-hand-side rings ( $r_c < x_k < r_c + d$ )  $R_f$  can be calculated in the following way. Let us denote the distance between a point of the external meniscus generatrix and the plane of the contact line by  $Q(x)$ —see Fig. 3. Then for  $x > r_c$  one has

$$Z_1 = \sqrt{R_f^2 - r_c^2} - Q(x). \quad [6]$$

The substitution of  $Z_r$  and  $Z_1$  from Eqs. [4] and [6] into Eq. [2] leads to

$$R_f^2 = r_c^2 + \left[ \frac{r_c^2 - D_k^2 - (x_k - d)^2}{2D_k} \right]^2, \quad r_c < x_k < r_c + d, \quad [7]$$

where

$$D_k = 1_k - Q(x_k) + h. \quad [8]$$

For the left-hand-side rings ( $r_c - d < |x_k| < r_c$ ), instead of Eq. [6], one has

$$Z_r = \sqrt{R_f^2 - r_c^2} - Q(x + d) - h. \quad [9]$$

Then the substitution of  $Z_1$  and  $Z_r$  from Eqs. [3] and [9] into Eq. [2] yields

$$R_f^2 = r_c^2 + \left[ \frac{r_c^2 - E_k^2 - x_k^2}{2E_k} \right]^2, \quad r_c - d < |x_k| < r_c, \quad [10]$$

where

$$E_k = 1_k - Q(x_k + d) - h. \quad [11]$$

Both Eqs. [7] and [11] reduce to Eq. [13] in Ref. (2) by means of the substitution  $x_k = x'_k + d/2$ ,  $h = 0$ .

The function  $Q(x)$  determines the profile of the liquid meniscus surrounding the bubble. The procedure for calculating  $Q(x)$  is given in the Appendix. It turns out that  $Q$  depends also on  $r_c$  and  $R_0$ :

$$Q = Q(x; r_c, R_0) \quad [12]$$

Then Eq. [7] or [10] yields  $R_f = R_f(x_k; h, r_c, R_0)$ . To find the most probable value of  $R_f$ , the dispersion

$\Psi(h, r_c, R_0)$

$$= \sum_{k=1}^N [\bar{R}_f - R_f(x_k; h, r_c, R_0)]^2, \quad [13]$$

was minimized numerically by means of the Hook–Jeeves method (8) (see also Ref. (6)). Here

$$\bar{R}_f = \sum_{k=1}^N R_f(x_k; h, r_c, R_0)/N \quad [14]$$

and the summation was carried out over all left and right hand side rings. The values of  $r_c$  and  $R_0$  corresponding to the minimum of  $\Psi$  in all cases are very close to the directly measured values of these quantities. For example, the difference between the calculated  $r_c$ , and  $r_c$  measured from a photograph of the inter-

ference pattern, like Fig. 2, did not exceed  $1\ \mu\text{m}$ . The respective difference for  $R_0$  is less than  $5\ \text{cm}$  ( $R_0$  ranges from 18 to 25 cm in our experiments). Of course, the relatively smaller accuracy of calculation of  $R_0$  is due to the slight effect  $R_0$  has on the interference pattern.

The independent calculation and measurement of  $r_c$  and  $R_0$  provide a control (and proof) of the accuracy of the differential interference measurements of  $R_f$ .

#### 4. ACCURACY OF THE INTERFEROMETRIC MEASUREMENTS

In contrast with the directly measured contact and equatorial radii  $r_c$  and  $R$ , the radius of curvature of the thin film,  $R_f$ , is measured indirectly by processing the data for the interference pattern, as explained above. To be certain about the reliability of the values of  $R_f$  thus obtained we checked the accuracy of the interferometric measurements in several independent ways.

As mentioned earlier (see also Ref. (2))  $R_f$  can be calculated independently from streaks and rings on the same photograph. Table II in Ref. (2) shows that the values of  $R_f$  calculated from streaks and rings coincide in the framework of the experimental accuracy. The latter is observed also with all processed photographs in the present study.

Another verification was presented in Ref. (5). The radii of curvature at the top of small aqueous and mercury drops of known size were measured interferometrically. The results show that there is no systematical error of the differential interference measurements in the range of curvatures studied (radii between 190 and  $310\ \mu\text{m}$ ). The inevitable random error is due mostly to the error involved by the measurements of the positions of the fringes of maximum or minimum intensity. The precision of these measurements is limited by the resolution power of the microscope (the latter is  $1\ \mu\text{m}$  for objective ( $\times 12.5$ ) as calculated from Eq. [97.8] of Ref. (18)). Because of the low reflectivity of the thin film, only the brightest parts of the fringes appear on the

photographs of bubbles. In fact this leads to an increase of the precision of measurement of the values of  $R_f$ .

We paid so much attention above to the analysis of the reliability of the differential interferometry measurements in Refs. (2, 5), because we believe that the existing controversy with the line tension measurements is to a large extent due either to the lack of such analysis or, whenever it is available, to its neglect when the experimental data are discussed. Instead, different *qualitative* arguments are invoked in order to explain the apparently incredible results. For example, Platikanov *et al.* (9) contended that "the values of the film tension  $\gamma$  are incorrectly determined in Ref. (10), probably because of wrongly measured  $R_f$ ." In Ref. (11) these authors specified that "when interpreting this interference picture one must also take into account the reflectivity of the lower bubble surface. This has not been done in Refs. (2, 10) and this could be one of the possible sources of systematic error."

Since these statements cast some doubt on our results, we will discuss below the possibility for the light reflected from the bottom of the bubble to distort the interference pattern from the film.

(i) The interference pattern, like that in Fig. 2 is due to light reflected from the "black" thin film. To verify that such a reflection is strong enough to be observable we formed a "bubble without bottom" by using film formed on the tip of a capillary—see Fig. 4. We observed the same interference pattern as with a bubble with the typical fringes: "streaks," "rings," and "moustaches." Hence, as low as the reflectivity of the thin film could be, it is high enough to create the observed interference pattern.

(ii) In our previous experiments (10) a microscope objective ( $\times 25$ ) with aperture number 0.5 and focal depth of  $2\ \mu\text{m}$  was used. The focal depth is about  $3\ \mu\text{m}$  with the objective ( $\times 12.5$ ) used in our experiments with the variable pressure cell (1). In both cases the focal depth is much smaller than the bubble diameter (the latter vary from 100 to  $600\ \mu\text{m}$

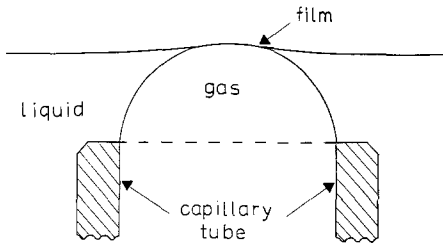


FIG. 4. Sketch of a thin foam film formed at the tip of a capillary that is immersed in a surfactant solution.

in our experiments). That is why it is possible to focus either at the film level or at the bottom of the bubble and the two images will not interfere. This is demonstrated by the following series of photographs (20, 21).

When focusing at the bottom of the bubble (point  $O_1$  in Fig. 1) we observe distinct interference "streaks" only with large bubbles ( $R > 150 \mu\text{m}$ )—see Fig. 5a. "Rings" and "moustaches" are not observed. When moving the

focus level upwards, the image from the bottom disappears and the picture becomes fuzzy. Only when a position, corresponding to point  $F_b$  in Fig. 1 is reached, can one again observe distinct image (Fig. 5b). This is the image of the illumination screen grid reflected from the bottom of the bubble. In fact point  $F_b$  is the focal point of the bubble bottom, which acts as a concave mirror.

The next distinct image (Fig. 5c) can be seen at the level of point  $F_r$ —the focus of the convex mirror, which is the thin liquid film. This image of the illumination grid confirms again the fact that reflections from the "black" thin film can be observed and recorded photographically. Finally, when focusing at the level of the film (point  $O_2$  in Fig. 1) we observe the already familiar interference pattern (Fig. 5d) due to the reflection from the film and meniscus surfaces.

(iii) Let us assume now that Platikanov *et al.* (11) are correct in claiming that the light

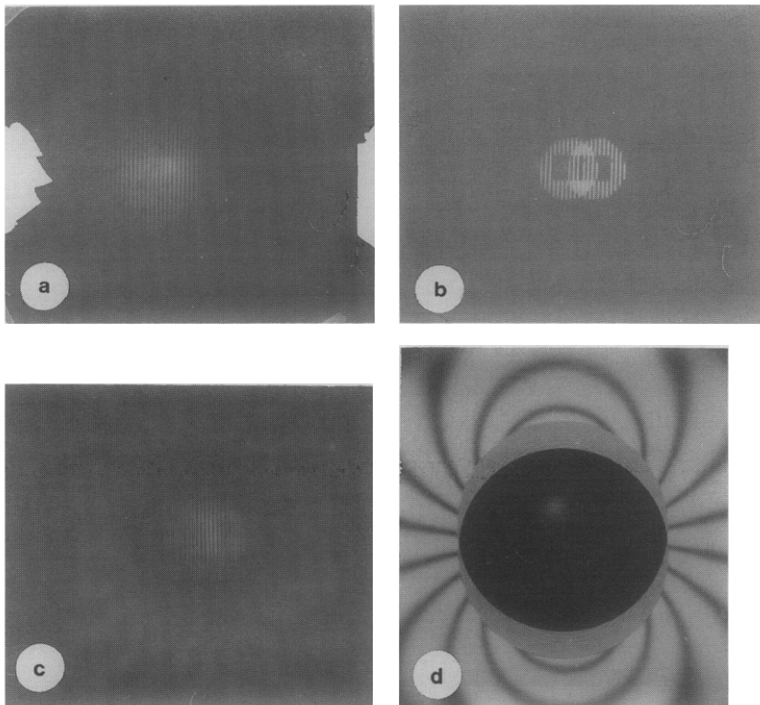


FIG. 5. Photographs of the images observed when focusing the microscope at the levels of the points  $O_1$  (a),  $F_b$  (b),  $F_r$  (c) and  $O_2$  (d), which are shown in Fig. 1.

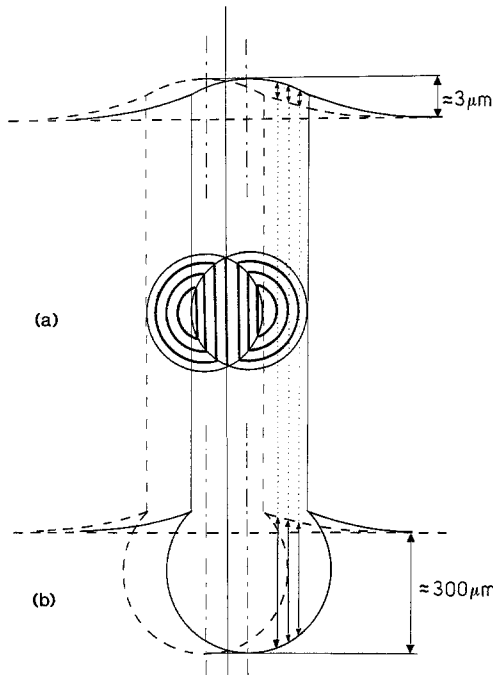


FIG. 6. Sketch of the differential interference pattern (in the middle) and of its interpretation (a) according to Ref. (2) and (b) according to Ref. (11).

reflected from the bottom of the bubble also contributes to the formation of the fringes observed at the film level. If such were the case, this light should interfere with the light reflected from the meniscus—see Fig. 6. We will show now that the interference pattern that should immerge is very different from that obtained by reflection from the film and no confusion nor superposition between the two is possible. It is observed experimentally that when the bubble diminishes all rings shrink with time and, one by one, disappear when they reach the inner contact line. The interference order of the rings due to reflection from the bubble bottom would be  $k \approx 4R/\lambda$ , where  $\lambda$  is the light wavelength. In accordance with Fig. 6b the rate of ring disappearing can be estimated as

$$\frac{dk}{dt} = \frac{4}{\lambda} \frac{dR}{dt} \quad [15]$$

By using the experimental data for  $dR/dt$

(note that they were obtained without using differential interferometry) one can calculate  $dk/dt$  from Eq. [15] and compare it with the rate of disappearance of the rings observed experimentally. The data presented in Table I demonstrate that the hypothesis for reflections from the bubble bottom is not confirmed: Eq. [15] predicts considerably faster movement of the rings than is observed experimentally. We have never observed such rapidly moving rings.

(iv) The experiment shows that each ring is matched at the contact line with a streak (or a moustache)—see Figs. 2 and 6. This is in agreement with our interpretation (the upper part of Fig. 6), corresponding to continuous reflecting surfaces (i.e., to gradual transition from the film to the outer meniscus). On the contrary, if the pattern is interpreted as shown at the lower part of Fig. 6, then the rings are not bound to match with the streaks (moustaches), because there is a discontinuity of the reflecting surfaces.

An additional method for verifying the reliability and precision of our interferometric measurements is presented below.

### 5. THE DOUBLE MIRROR METHOD

Both Fig. 5b and 5c represent images of the same object—the illumination screen grid. However, they have different sizes because they were obtained from two spherical “mirrors” (the bottom of the bubble and the film) of different curvatures. In general, if  $l_i$  is some characteristic length of an image produced by a spherical mirror of radius  $R_i$ , then

TABLE I  
Rate of Interference Rings Disappearance  
in Seconds per Ring

$R_f$ [ $\mu\text{m}$ ]	Calculated from Eq. [15]	Experimental values
155	3.3	980
100	2.1	320
60	0.5	36

$$\frac{l_1}{l_2} = \frac{R_1}{R_2} \quad [16]$$

It is supposed in Eq. [16] that the subject is far enough from the mirrors, as it is in our case. Equation [16] provides a simple method (20, 21) for measuring the curvature of the film if the curvature  $b$  of the bubble bottom is known

$$R_f = \frac{l_f}{l_b} b, \quad [17]$$

where  $l_f$  and  $l_b$  are liable to direct measurement (the subscripts "f" and "b" refer to the mirrors due to the film and the bubble bottom, respectively).  $b$  is calculated from the directly measured equatorial radius  $R$  by means of Eq. [A.4] or numerically—see Appendix.

In our experiments  $l_f$  and  $l_b$  were the respective images of the (shortest) distance between the two openings of the illumination slit—see Fig. 7. The three parameters in the right-hand side of Eq. [16] were recorded experimentally as functions of time in the following way. At suitably chosen time intervals photographs of the images formed by the two "mirrors" were taken. In addition, visual measurements of  $R$  and interferometric measurements of  $R_f$  (from streaks) were carried out periodically, as described in Ref. (10). The illumination slit was exchanged with the illumination grid of constant  $48 \mu\text{m}$  during the

interferometric measurements of  $R_f$ . Monochromatic light ( $\lambda = 546 \text{ nm}$ ) and black and white photographic film of sensitivity 6 ASA (HR II Fuji) were used. The exposure time used when taking photographs of  $l_b$  and  $l_f$  was 4 and 15 s, respectively. The plots of  $l_b$  vs  $b$  and  $l_f$  vs  $R_f$  turned out to be straight lines passing through the coordinate origin. (The existence of nonzero intersect would be an indication that the image had been overexposed or underexposed.)

In Fig. 8  $R_f$  is plotted vs time. The filled and the open circles are obtained by means of the interferometric and the double mirror method. The random error of the double mirror method turned out to be higher. One sees that the results of the two methods are in very good agreement. This fact in conjunction with the results of the previous section demonstrates that there are no reasons for any doubt about the reliability of the interferometric measurements of  $R_f$ .

## 6. EXPERIMENTAL RESULTS AND DISCUSSION

The vertical and the horizontal projections of the Neumann—Young force balance provide two equations for independent calculation of the film tension,  $\gamma$ , and the line tension,  $\kappa$  (see Eqs. [6]–[7] in Ref. (10)):

$$\gamma = \sigma(\sin \varphi_c + \sin \psi_c) / \sin \theta \quad [18]$$

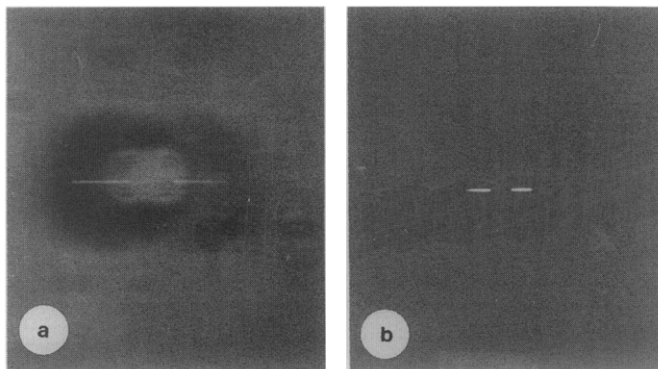


FIG. 7. Photograph of the image of the illumination slit reflected from the thin film (a) and from the bubble bottom (b).

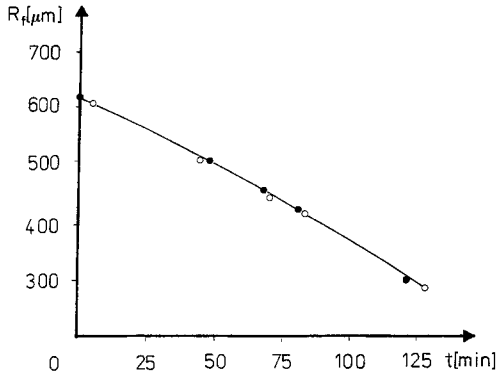


FIG. 8. Radius of thin film curvature,  $R_f$  vs time  $t$ : data from differential interference measurements (●) and from the double mirror method (○).

$$\kappa = \sigma r_c [\cos \varphi_c + \cos \psi_c - (\sin \varphi_c + \sin \psi_c) \cot \theta]. \quad [19]$$

Here  $\sigma$  is the solution surface tension,

$$\theta = \arcsin(r_c/R_f), \quad [20]$$

and the angles  $\varphi_c$  and  $\psi_c$  are calculated as described in the Appendix from the experimental values of  $r_c$  and  $R$ .

The experimental data presented below are obtained with “stopped” bubbles, i.e., at fixed equatorial radius  $R$ . During the experiments the temperature was kept  $(22 \pm 0.5)^\circ\text{C}$ . We used two solutions: with 0.25 and 0.32 mol/liter NaCl, both of them containing  $1.73 \times 10^{-3}$  mol/liter sodium dodecyl sulfate. The surface tension,  $\sigma$ , of the solutions was 32.4 and 31.7 mN/m, respectively.

The coordinate origin in Figs. 9–11 corresponds to the time moment when the equatorial radius of an initially shrinking bubble is fixed by regulation of the pressure inside the experimental cell. The relaxations of  $r_c$  and  $R_f$  of a stopped bubble were measured as described in Section 3. After processing the data,  $\gamma$  and  $\kappa$  were calculated by using Eqs. [18] and [19].

The open and the filled circles in Fig. 9 are measured with two stopped bubbles of radii  $R = 282 \mu\text{m}$  and  $R = 265 \mu\text{m}$ , respectively. The filled and open triangles correspond to two smaller bubbles, both of them of radius

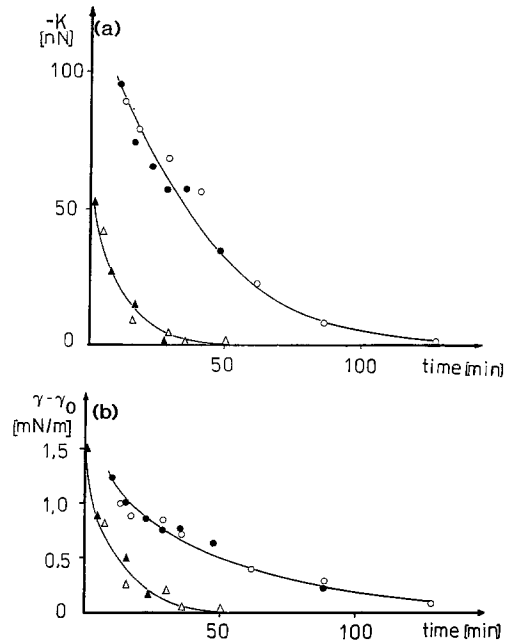


FIG. 9. Relaxation of the line tension  $\kappa$  (a) and of the film tension  $\gamma$  (b) with time  $t$  at fixed equatorial bubble radius: open circles,  $R = 282 \mu\text{m}$ ; filled circles,  $R = 265 \mu\text{m}$ ; open and filled triangles, two bubbles each of radius  $R = 152 \mu\text{m}$  (0.25 mol/liter NaCl).

$R = 152 \mu\text{m}$ . Each of these four bubbles has been formed in the solution with 0.25 mol/liter NaCl. Each point corresponds to a photograph of the differential interference pattern. The data demonstrates that both the film tension,  $\gamma$ , and the line tension,  $\kappa$ , exhibit relax-

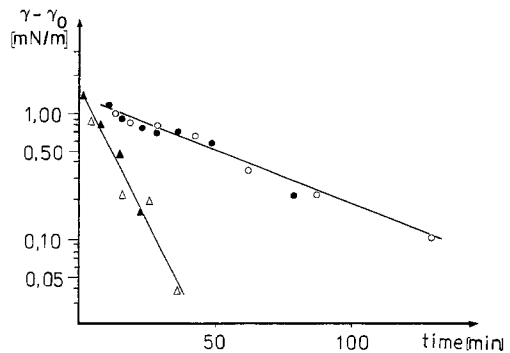


FIG. 10. The data for the film tension  $\gamma$  from Fig. 9b presented in a log scale vs time  $t$ .

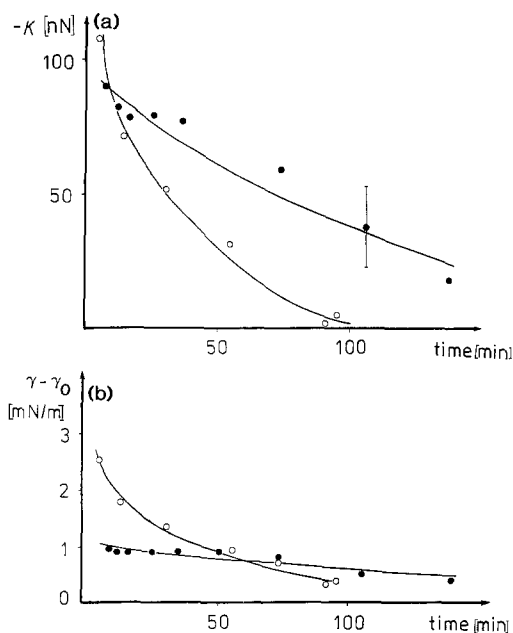


FIG. 11. Relaxation of the line tension  $\kappa$  (a) and of the film tension  $\gamma$  (b) with time  $t$  at fixed equatorial bubble radius: open circles,  $R = 185 \mu\text{m}$ ; filled circles,  $R = 282 \mu\text{m}$  (0.32 mol/liter NaCl).

ation with time.  $\kappa$  tends to zero in the framework of the experimental accuracy.  $\gamma$  tends to its equilibrium value  $\gamma_0 = 64.4 \text{ mN/m}$ , measured by de Feijter (12) with macroscopic rectangular films. Obviously the smaller bubbles relax faster than the larger ones.

Figure 10 represents the same data as in Fig. 9b, but with a log scale on the ordinate axis. The slope yields a relaxation time  $\tau_1 \approx 50 \text{ min}$  for the larger bubbles and  $\tau_2 \approx 10 \text{ min}$  for the smaller bubbles. The respective contact radii measured after relaxation was complete are  $r_{c1} = 85 \mu\text{m}$  and  $r_{c2} = 37 \mu\text{m}$ . It is interesting to note that  $\tau_2/\tau_1 \approx r_{c2}^2/r_{c1}^2 \approx 0.19$ . The relaxation times calculated from the data for  $\kappa$  (Fig. 9a) coincide with  $\tau_1$  and  $\tau_2$  as determined from the relaxation of  $\gamma$  (Fig. 9b).

Figure 11 represents analogous data for the solution with 0.32 mol/liter NaCl. The equilibrium film tension in this case is  $\gamma_0 = 62.7 \text{ mN/m}$  (12). The filled and the open circles correspond to stopped bubbles with  $R = 282$  and  $185 \mu\text{m}$ , respectively. The relaxation times

determined from these two curves are  $\tau_1 = 130 \text{ min}$  and  $\tau_2 = 36 \text{ min}$ . Again  $\tau_2/\tau_1 \approx r_{c2}^2/r_{c1}^2 \approx 0.26$  ( $r_{c1} = 100 \mu\text{m}$ ,  $r_{c2} = 500 \mu\text{m}$ ), i.e., the larger the film area, the longer the relaxation.

The observed relaxation processes are probably due to some deviation from equilibrium brought about the shrinking of the bubble. However, this is not a simple effect like relatively slow surfactant desorption during the shrinking, which can cause a decrease of the bubble surface tension. The latter effect has been already discussed and ruled out—see Ref. (10), p. 139.

The general conclusion from the present work is that the film and line tension,  $\gamma$  and  $\kappa$  of small floating bubbles have nonequilibrium dynamic values when the three-phase contact line shrinks (advancing meniscus). They are in agreement with the findings in Ref. (1) that the contact angle,  $\alpha$ , of a shrinking bubble acquires nonequilibrium values. This does not mean, that the values of  $\gamma$  and  $\kappa$  so measured are meaningless. They are real film and line tensions, but since the system is out of equilibrium, they are determined, at least in part, by dynamic phenomena. In this respect they are analogous to the "dynamic interfacial tension" and "dynamic contact angle." That is why we believe it pertinent to introduce the concept of "dynamic line tension." It is worthwhile noting that the equilibrium line tension, as predicted by the theory (13, 16), is an extremely small quantity (of the order of  $10^{-11}$ – $10^{-12} \text{ N}$ ), so that it usually turns out to be below the threshold of the experimental accuracy. On the other hand, the dynamic line tension can be many orders of magnitude greater; it can affect the value of the contact angle and the processes accompanying the motion of a three-phase contact line. The processes giving rise to the dynamic line tension deserve a separate study. They are probably connected with local alterations of the interfacial shapes and tensions in a narrow vicinity of the three-phase contact zone. We believe the study of these effects will be stimulated by their importance for the occurrence

of many phenomena like wetting, spreading, interactions of fluid particles, and biological cells.

The contact angle  $\alpha$  and the film and line tensions  $\gamma$  and  $\kappa$  are connected during the relaxation by

$$\frac{1}{\cos(\alpha/2)} - \frac{2\sigma}{\gamma} + \frac{\kappa}{\gamma r_c} = 0; \quad [21]$$

cf. Eq. [1] in Ref. (1). The data in Fig. 11 (the larger bubble) shows that the change of the first term in Eq. [21] during the relaxation is  $-0.0015$ , of the second term is  $+0.0145$ , and of the third term is  $+0.0159$ . The conclusion is that the variations of the film and line tensions counterbalance each other in order the equilibrium condition, Eq. [21], to be satisfied. This confirms again our finding from Ref. (10) that the variation of the  $\cos \alpha$  term in [21] is negligible in comparison with the variations of the two other terms. The pronounced changes of  $\gamma$  and  $\kappa$  make it impossible to calculate the line tension from Eq. [21] as proposed by Platikanov *et al.* (9, 15). In contrast to our experimental findings these authors hypothesized that both  $\gamma$  and  $\kappa$  are constants during the bubble shrinking. Recently (22) they tried to confirm their hypothesis by direct measurements of the film tension of shrinking bubbles by using a method similar to the one described in Section 5 above. Apparently, they were able to show that the film tension is independent of the bubble's radius and, thereby, of the time. However, this conclusion is due to misinterpretation of the experimental data. While their measurements of the radius of curvature of the film do not raise serious objections, the calculation of the film tension is based on a wrong force balance:

$$\frac{2\sigma}{b} = \frac{2\gamma}{R_f}. \quad [22]$$

This equation is missing a hydrostatic pressure term. The correct balance is (see, e.g., Ref. (23) or Ref. (10), Eq. [12])

$$\frac{2\sigma}{b} = \frac{2\gamma}{R_f} - \rho g L, \quad [23]$$

where  $L$  is the distance (along the vertical) between the levels of the bubble bottom and the solution surface (far from the bubble),  $\rho$  is the solution density and  $g$  is the gravity acceleration. Figure 12 is a modified version of their Fig. 7. The points are calculated by them using Eq. [22] and the horizontal line is their average value of  $\gamma$ . To illustrate the effect of the gravity term, we have recalculated their data points lying close to the horizontal line by using the correct equation [23]. These data are shown by triangles and, not surprisingly, the shape of the curve drawn through them is very similar to our curve  $\gamma$  vs  $t$  in Figs. 9b and 11b. This is an indication that their data also confirm our finding about the nonequilibrium nature of the measured film tension of shrinking bubbles. It is also worthwhile noting that for large bubbles the film tension turns out to be larger than  $2\sigma$ . This is also in agreement with our present and previous (10) results and does not substantiate the claims in Ref. (11) that "the measurements of  $\gamma$  in Ref. (10) are not correct."

## 7. CONCLUDING REMARKS

(i) The new experiments with small air bubbles described in this paper confirm the large values of the film and line tension ( $\gamma >$

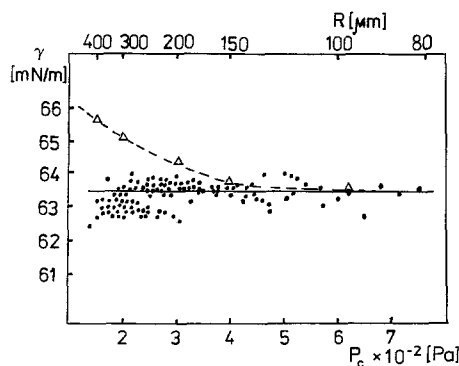


FIG. 12. Plot of the film tension  $\gamma$  vs the capillary pressure  $P_c$ . The points are calculated in Ref. (22) from experimental data by using Eq. [22]; their mean value is prescuted by the solid line. The latter transforms into the dashed line after a recalculation based on the correct Eq. [23].

$2\sigma, \kappa \sim -100 \text{ nN}$ ) measured in Ref. (10) with shrinking bubbles formed in 0.05% aqueous solutions of sodium dodecyl sulfate at 0.25 and 0.32 mol/liter added NaCl (see the values of  $\gamma$  and  $\kappa$  in Figs. 9–11 at the earlier times).

(ii) Similar to the contact angle  $\alpha = \varphi_c - \psi_c$ , the film and line tensions,  $\gamma$  and  $\kappa$ , of the stopped bubble exhibit a relaxation. The relaxation time is longer with the larger bubbles— see Figs. 9–11.

(iii) The relaxing line tension  $\kappa$  tends to zero in the framework of the experimental accuracy ( $\pm 15 \text{ nN}$ ). This experimental finding is compatible with the theoretical result of de Feijter and Vrij (13), who calculated  $\kappa = -0.001 \text{ nN}$  for equilibrium Newton black films.

(iv) The relaxing film tension  $\gamma$  tends to an equilibrium value, which agrees well with the value measured by de Feijter (12) with macroscopic equilibrium films.

(v) The results for  $\gamma$  are also in agreement with the experiments of Platikanov *et al.* (11, 14), who recovered de Feijter’s equilibrium values of  $\gamma$  in experiments with bubbles fixed at the tip of a capillary (immobile contact line).

(vi) A thorough check of the differential interferometry used in this study showed that it is a reliable and precise. The determined variations of  $\gamma$  and  $\kappa$  are real effects; they are not artifacts due to some systematic errors of the interferometric technique, as suggested in Refs. (9, 11).

(vii) The results from the present study suggest that under dynamic conditions a “dynamic line tension,” analogous to the “dynamic interfacial tension” should act at the three-phase contact line.

APPENDIX

CALCULATION OF ANGLES  $\varphi_c, \psi_c$ , AND OF THE MENISCUS PROFILE

(a) Profile of the Lower Bubble Surface

The lower bubble surface (situated between the planes  $z = 0$  and  $z = z_c$  in Fig. 1) is de-

formed by gravity. In this case the Laplace equation

$$\frac{1}{x} \frac{d}{dx} (x \sin \varphi) = \frac{2}{b} + q^2 z \quad [A.1]$$

has no closed analytical solution. In [A.1]  $\varphi$  is running slope angle of the bubble surface generatrix

$$\frac{dz}{dx} = -\tan \varphi, \quad [A.2]$$

$b$  is the radius of curvature at the bubble bottom, and

$$q = \sqrt{\frac{\Delta\rho g}{\sigma}} \quad [A.3]$$

has a dimension of inverse length;  $\Delta\rho$  is the difference between the mass densities of the liquid and gas phases,  $g$  is gravity acceleration and  $\sigma$  is the surface tension of the solution.

In our case  $q, r_c$ , and  $R$  are supposed to be known. Then  $b$  can be determined by using the equation

$$b = R \left[ 1 - \frac{q^2 b^2}{6} + \frac{q^4 b^4}{6} (\ln 2 - 1/6) \right]^{-1}, \quad [A.4]$$

which is valid for  $qb \ll 1$ —see Ref. (2). Since our experiments  $R < 300 \mu\text{m}$ , then  $qb < 0.15$  and Eq. [A.4] holds with a good precision. (The error of calculation in  $b$  is less than  $0.2 \mu\text{m}$  for the largest bubbles.) Equations [A.1] and [A.2] form a set of two ordinary differential equations for the functions  $x(\varphi)$  and  $z(\varphi)$ . This set is integrated numerically by using the RKF45 procedure based on Runge–Kutta method (19). The integration starts from the bubble bottom ( $\varphi = \pi, x(\pi) = 0, z(\pi) = 0$ ) and proceeds with appropriate increments in  $\varphi$  up to the point  $x = r_c, \varphi = \varphi_c, z = z_c$ . In this manner  $\varphi_c$  and  $z_c$  are determined from the known values of  $r_c$  and  $R$ —see Fig. 1.

Instead of Eq. [A.4] a similar procedure can be used to determine  $b$ . The integration of Eqs. [A.1]–[A.2] starts from the bubble bottom

(with a trial value of  $b$ ) and is carried out up to the point  $\varphi = \pi/2$ . The procedure is repeated with different  $b$  until the experimental value of  $R$  is found at  $\varphi = \pi/2$ .

The volume of the solution,  $V_b$ , which is displaced by the bubble, is calculated in the following way:

$$V_b = \pi \int_0^{z_c} x^2(z) dz = \pi r_c^2 z_c - 2\pi \int_0^{z_c} zx(z) \frac{dx}{dz} dz. \quad [A.5]$$

On the other hand, by integration of Eq. [A.1] one obtains

$$r_c \sin \varphi_c = \frac{r_c^2}{b} + q^2 \int_0^{z_c} zx(z) \frac{dx}{dz} dz. \quad [A.6]$$

The elimination of the integral term between Eqs. [A.5] and [A.6] yields (17):

$$V_b = 2\pi \frac{r_c}{q^2} \left( \frac{1}{2} q^2 r_c z_c + \frac{r_c}{b} - \sin \varphi_c \right). \quad [A.7]$$

*(b) Profile of the Convex Liquid Meniscus*

As mentioned earlier, the studied small shrinking bubbles are kept immobile at the top of a convex liquid meniscus. The subject of our interest below is the shape of this meniscus after the disappearance of the bubble—see Fig. 13. The radius of curvature at the top of the meniscus,  $R_0$ , as well as the outer radius of the glass cylindrical container,  $r_0$ , are supposed to be known. The meniscus profile sat-

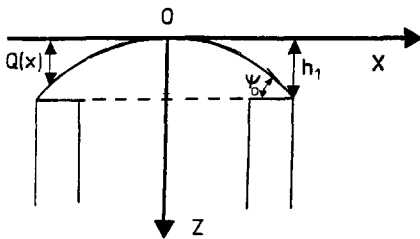


FIG. 13. Sketch of the convex liquid meniscus in the cylindrical glass container after the disappearance of the bubble.

isfies a set of equations similar to Eqs. [A.1]–[A.2],

$$\frac{1}{x} \frac{d}{dx} (x \sin \theta) = \frac{2}{R_0} + q^2 z \quad [A.8]$$

$$\frac{dz}{dx} = \tan \theta, \quad [A.9]$$

where  $\theta$  is the running slope angle. Equations [A.8]–[A.9] are integrated numerically from the meniscus apex ( $\theta = 0, x(0) = z(0) = 0$ —see Fig. 13) down to the point  $x = r_0, \theta = \theta_0, z = h_0$  at the edge of the glass container. In this way  $\theta_0$  and  $h_0$  are determined from the known  $R_0$  and  $r_0$ —see Fig. 13. The meniscus volume can be expressed as

$$V_0 = 2\pi \frac{r_0}{q^2} \times \left( \frac{1}{2} q^2 r_0 h_0 + \frac{r_0}{R_0} - \sin \theta_0 \right). \quad [A.10]$$

Equation [A.10] is a counterpart of Eq. [A.7].

*(c) Profile of the Meniscus around the Bubble*

Let us now consider the case when there is a bubble at the top of the convex meniscus—Fig. 14. Our aim is to determine the angle  $\psi_c$  and the function  $Q(x)$  governing the shape of the meniscus. The Laplace equation in this case can be presented in the form

$$\frac{1}{x} \frac{d}{dx} (x \sin \psi) = \Delta P / \sigma + q^2 Q(x), \quad [A.11]$$

where  $\psi$  is the respective running slope angle,

$$\frac{dQ}{dx} = \tan \psi, \quad [A.12]$$

$\Delta P$  is the capillary pressure drop across the meniscus surface at the level  $z = 0$  ( $Q = 0$ )—see Fig. 14. Taking into account the capillary pressure drops across the thin film and across the bottom of the bubble  $\Delta P$  is expressed in the form

$$\Delta P = \frac{2\gamma}{R_f} - \frac{2\sigma}{b} - \Delta \rho g z_c. \quad [A.13]$$

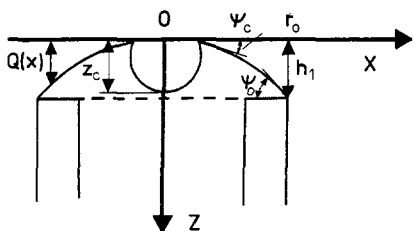


FIG. 14. Sketch of the convex liquid meniscus with a small bubble attached at its apex.

On the other hand, the vertical projection of the Neumann–Young force balance equation yields

$$\gamma \frac{r_c}{R_f} = \sigma \sin \varphi_c + \sigma \sin \psi_c; \quad [A.14]$$

see also Fig. 1. The combination of Eqs. [A.13]–[A.14] leads to

$$\Delta P / \sigma = \frac{2}{r_c} (\sin \varphi_c + \sin \psi_c) - \frac{2}{b} - q^2 z_c. \quad [A.15]$$

We suppose that  $r_c$  and  $r_0$  are known and that  $\varphi_c$ ,  $z_c$ ,  $b$ ,  $V_b$ , and  $V_0$  are calculated as described above. Then the volume

$$V_1 = V_b + V_0 \quad [A.16]$$

is also known. In addition, similar to Eq. [A.5], it is easy to derive

$$V_1 = \pi r_c^2 h_1 - 2\pi \int_{r_c}^{r_0} Q(x) x dx; \quad [A.17]$$

see Fig. 14 for the notation. An integration of Eq. [A.11] yields

$$\int_{r_c}^{r_0} Q(x) x dx = \frac{1}{q^2} \left[ \frac{1}{2} \frac{\Delta P}{\sigma} (r_c^2 - r_0^2) + r_0 \sin \psi_0 - r_c \sin \psi_c \right]. \quad [A.18]$$

A substitution from Eqs. [A.15]–[A.17] into Eq. [A.18] leads to

$$\begin{aligned} \sin \psi_c = \frac{r_c}{r_0} & \left[ q^2 \frac{V_b + V_0}{2\pi r_0} + \sin \psi_0 \right. \\ & - \frac{1}{2} q^2 r_0 h_1 + \frac{1}{r_0} (r_0^2 - r_c^2) \\ & \left. \times \left( \frac{1}{2} q^2 z_c + \frac{1}{b} - \frac{\sin \varphi_c}{r_c} \right) \right]. \quad [A.19] \end{aligned}$$

The angle  $\psi_c$  and the function  $Q(x)$  are calculated in the following way. At given  $r_0$  and  $r_c$  the parameters  $\psi_0$  and  $h_1$  are functions of  $\psi_c$ , i.e.,

$$\psi_0 = \psi_0(\psi_c) \quad \text{and} \quad h_1 = h_1(\psi_c), \quad [A.20]$$

the values of the latter two functions for a given  $\psi_c$  are calculated by numerical integration of Eqs. [A.11]–[A.12] from the top of the meniscus ( $x = r_c$ ,  $\psi = \psi_c$ ,  $Q = 0$ ) down to the point  $x = r_0$ , where  $\psi = \psi_0$  and  $Q = h_1$ . In view of Eq. [A.20], Eq. [A.19] allows calculation of the angle  $\psi_c$  at known  $r_c$ ,  $r_0$ ,  $q$ ,  $V_b$ ,  $V_0$ ,  $b$ ,  $z_c$ , and  $\varphi_c$ . We solved Eq. [A.19] numerically by using trial values for  $\psi_c$ . A good zeroth approximation for  $\psi_c$  is obtained by substituting  $\psi_0 = \theta_0$  and  $h_1 = h_0$  in the right-hand side of Eq. [A.19].

#### REFERENCES

1. Ivanov, I. B., Dimitrov, A. S., Nikolov, A. D., Denkov, N. D., and Kralchevsky, P. A., *J. Colloid Interface Sci.* **151**, 446 (1992).
2. Nikolov, A. D., Kralchevsky, P. A., and Ivanov, I. B., *J. Colloid Interface Sci.* **112**, 122 (1986).
3. Beyer, H., "Theorie und Praxis der Interferenzmikroskopie." Akademische Verlagsgesellschaft, Leipzig, 1974.
4. Beyer, H., *Jenaer Rundsch.* **16**, 82 (1971).
5. Nikolov, A. D., Dimitrov, A. S., and Kralchevsky, P. A., *Optica Acta* **33**, 1359 (1986).
6. Dimitrov, A. S., Kralchevsky, P. A., Nikolov, A. D., and Wasan, D. T., *Colloids Surf.* **47**, 299 (1990).
7. Lobo, L. A., Nikolov, A. D., Dimitrov, A. S., Kralchevsky, P. A., and Wasan, D. T., *Langmuir* **6**, 995 (1990).
8. Hook, R., and Jeeves, T. A., *J. Assn. Comp. Mach.* **8**, 212 (1961).
9. Toshev, B. V., Platikanov, D., and Scheludko, A., *Langmuir* **4**, 489 (1988).

10. Kralchevsky, P. A., Nikolov, A. D., and Ivanov, I. B., *J. Colloid Interface Sci.* **112**, 132 (1986).
11. Platikanov, D., Nedyalkov, M., Scheludko, A., and Toshev, B. V., *J. Colloid Interface Sci.* **121**, 100 (1988).
12. de Feijter, J. A., Ph.D. Thesis. University of Utrecht, 1973; de Feijter, J. A., and Vrij, A., *J. Colloid Interface Sci.* **64**, 269 (1978).
13. de Feijter, J. A., and Vrij, A., *J. Electroanal. Chem.* **47**, 9 (1972).
14. Platikanov, D., Nedyalkov, M., and Rangelova, N., *Colloid Polym. Sci.* **265**, 72 (1987).
15. Platikanov, D., Nedyalkov, M., and Nasteva, V., *J. Colloid Interface Sci.* **75**, 620 (1980).
16. Tarazona, P., and Navascues, G., *J. Chem. Phys.* **75**, 3114 (1981).
17. Hartland, S., and Hartley, R. W., "Axisymmetric Fluid-Liquid Interfaces." Elsevier, Amsterdam, 1976.
18. Landsberg, G. S., "Optica," p. 346-357. Nauka, Moskow, 1976. (in Russian)
19. Forsythe, G. E., Malcolm, M. A., and Moler, C. B., "Computer Methods for Mathematical Computations." Prentice-Hall, Englewood Cliffs, NJ, 1977.
20. Ivanov, I. B., Paper presented at the Pre-Conference Congress on "Dispersed Systems and Biocolloids," Tsukuba, 1988.
21. Ivanov, I. B., Paper presented at the 7th International Symposium "Surfactants in Solution," Ottawa, 1988.
22. Nedyalkov, M., Schoppe, G., and Platikanov, D., *Colloids Surf.* **47**, 95 (1990).
23. Princen, H. M., *J. Colloid Sci.* **18**, 178 (1963).